INTERNATIONAL JOURNAL FOR NUMERICAL METHODS IN FLUIDS, VOL. 19, 105–134 (1994)

NUMERICAL SIMULATION OF COOLING-INDUCED CONVECTIVE CURRENTS ON A LITTORAL SLOPE

G. M. HORSCH

Institute of Nuclear Technology and Radiation Protection, National Center for Scientific Research 'Democritos', 153 10 Aghia Paraskevi, Athens, Greece

H. G. STEFAN

St. Anthony Falls Hydraulic Laboratory, Department of Civil & Mineral Engineering, University of Minnesota, Minneapolis, MN 55414, U.S.A.

AND

S. GAVALI

Fujitsu America, 3055 Orchard Drive, San Jose, CA 95134, U.S.A.

SUMMARY

The transient development of cooling-induced flow in a triangular domain filled with water is studied by means of numerical simulation as a model for flow developing in the littoral region of lakes or coasts. The domain is fitted in polar co-ordinates; solutions are obtained for different values of the independent parameters of the model, which are the Rayleigh number (*Ra*), the Prandtl number (*Pr*) and the slope of the domain (*S*). Within the ranges examined, as *Ra* is increased, different regimes of the developing flow are observed; these are found qualitatively to be insignificantly influenced by changes in *S*, whereas the flow is found to be quantitatively insensitive to *Pr* for high enough values of *Pr*. Several interesting features of the flow are depicted and integral values useful in the analysis of flow in lakes are extracted.

KEY WORDS Numerical simulation Transient Cooling-induced currents Littoral slope

1. INTRODUCTION

Cooling of surface waters which lie on a slope, such as those in the littoral region of lakes or in coasts, has been shown by Stefan *et al.*[1] to result, under favourable conditions, in the development of horizontal gravitational flow. The sloping bed topography plays a key role in the development of the horizontal temperature gradient which drives the flow, since shallower water cools faster than deeper water. A noteworthy feature of this setting is that the horizontal temperature gradient develops as a result of the internal flow balance rather than being externally imposed. This feature is shared by the flow developing during the heating cycle of lakes.[2] Given the time scale of forcing (cooling) in nature, the 'littoral circulation' problem (as the above-described flow will be referred to below) is an essentially unsteady flow problem.

In order to simulate the cooling-induced convective currents on an idealized slope, Horsch and Stefan[3] formulated a model of unsteady natural convection in a triangular enclosure. The model has as independent parameters the Rayleigh number (*Ra*), the Prandtl number (*Pr*) and

CCC 0271-2091/94/140105-30

Received 1 June 1993
Revised 28 December 1993

the slope (S) of the littoral zone. Horsch and Stefan[3] presented a numerical solution to the model in a domain fitted in Cartesian co-ordinates for a single value of the triplet Ra, Pr, S and documented a variety of intriguing features of the inception and development of the circulation at a relatively high Ra-value ($Ra = 10^8$). The major features were in agreement with their laboratory visualization experiment. Among them is the emergence and disappearance of convective Bénard-like cells during the evolution of the flow.

Natural convective flows in enclosures have received extensive attention in the literature because of their importance in several disciplines.[4] Two archetypal settings are the Bénard problem (see e.g. Reference 5) and the rectangle with differentially heated end walls (see e.g. Reference 6). The problem examined herein shares features with both these problems. Cooling of the top surface entails the potential for physical instability (as in the Bénard problem); the development of a horizontal temperature gradient drives the horizontal circulation (as in the rectangle with differentially heated end walls). The complexity of the 'littoral zone' flow, caused by the particular boundary conditions pertinent to this physical problem, can be brought out by comparing it to flow forced by 'attic space' boundary conditions in a similar triangular geometry. The latter flow has been shown by Poulikakos and Bejan[7] to evolve, in the range of parameters they examined, to a single-cell configuration through a regular spin-up; this evolution is devoid of convective cells.

The focus in the present examination of the novel 'littoral slope' flow is on establishing the qualitative features of the transient development of the flow over a wide range of the governing parameters rather than on producing definitively accurate solutions. To this end, some implications of a problem formulation similar to that of Horsch and Stefan[3] are first analysed. Then numerical solutions of the time-dependent problem are obtained in a domain fitted in polar rather than Cartesian co-ordinates in order to rid the solutions of numerical errors that cannot be quantified. These solutions are obtained over a range of values of Ra, Pr and S, which makes it possible to identify a variety of different regimes and also to draw conclusions about the pertinence of the simulation to the actual littoral exchange problem.

2. THE NUMERICAL MODEL

2.1. Governing equations

The numerical model is formulated in terms of the equations of continuity, momentum and energy, all expressed in polar co-ordinates, in which the boundary of the domain can be fitted naturally:

momentum equations

$$\frac{\partial u}{\partial t} + v\frac{\partial u}{\partial r} + \frac{u}{r}\frac{\partial u}{\partial \theta} + \frac{uv}{r} = -\frac{1}{\rho_0}\frac{1}{r}\frac{\partial p}{\partial \theta} + \nu\left[\frac{1}{r}\frac{\partial}{\partial r}\left(r\frac{\partial u}{\partial r}\right) + \frac{1}{r^2}\frac{\partial^2 u}{\partial \theta^2}\right] + \nu\left(-\frac{u}{r^2} + \frac{2}{r^2}\frac{\partial v}{\partial \theta}\right) + g\beta(T_0 - T)\cos\theta, \tag{1}$$

$$\frac{\partial v}{\partial t} + v\frac{\partial v}{\partial r} + \frac{u}{r}\frac{\partial v}{\partial \theta} - \frac{u^2}{r} = -\frac{1}{\rho_0}\frac{\partial p}{\partial r} + \nu\left[\frac{1}{r}\frac{\partial}{\partial r}\left(r\frac{\partial v}{\partial r}\right) + \frac{1}{r^2}\frac{\partial^2 v}{\partial \theta^2}\right] - \nu\left(\frac{v}{r^2} + \frac{2}{r^2}\frac{\partial u}{\partial \theta}\right) + g\beta(T_0 - T)\sin\theta, \tag{2}$$

continuity equation

$$\frac{1}{r}\frac{\partial}{\partial r}(rv) + \frac{1}{r}\frac{\partial u}{\partial \theta} = 0, \tag{3}$$

energy equation

$$\frac{\partial T}{\partial t} + v\frac{\partial T}{\partial r} + \frac{u}{r}\frac{\partial T}{\partial \theta} = \alpha\left[\frac{1}{r}\frac{\partial}{\partial r}\left(r\frac{\partial T}{\partial r}\right) + \frac{1}{r^2}\frac{\partial^2 T}{\partial \theta^2}\right], \tag{4}$$

where $u = u(r, \theta)$ is the tangential velocity, $v = v(r, \theta)$ is the radial velocity, p is the pressure, T_0 is the initial temperature, ν is the kinematic viscosity, β is the thermal expansivity, g is the acceleration due to gravity and α is the thermal diffusivity. In these equations the Boussinesq approximation has been implemented and in the body force the density has been expressed as a linear function of the temperature. This formulation of the density has implications for the occurrence of a quasi-steady state as discussed below.

The boundary conditions, shown in Figure 1, are

shear-free surface with heat transfer

$$u = 0; \quad \frac{\partial v}{\partial \theta} = 0; \quad \frac{k}{r}\frac{\partial T}{\partial \theta} = H \quad \text{at } \theta = 0, \quad 0 < r \leqslant R, \tag{5}$$

no-slip, adiabatic boundaries at bottom and end of domain

$$u = 0, \quad v = 0, \quad \frac{\partial T}{\partial \theta} = 0 \quad \text{at } \theta = \theta_T, \quad 0 < r \leqslant R, \tag{6}$$

$$u = 0, \quad v = 0, \quad \frac{\partial T}{\partial r} = 0 \quad \text{at } r = R, \quad 0 \leqslant \theta \leqslant \theta_T, \tag{7}$$

where k is the conductivity, H is the imposed surface heat loss and R and θ_T specify the size of the domain shown in Figure 1. The above conditions imply that there is no wind shear on the water surface and no heat transfer from or into the sediments.

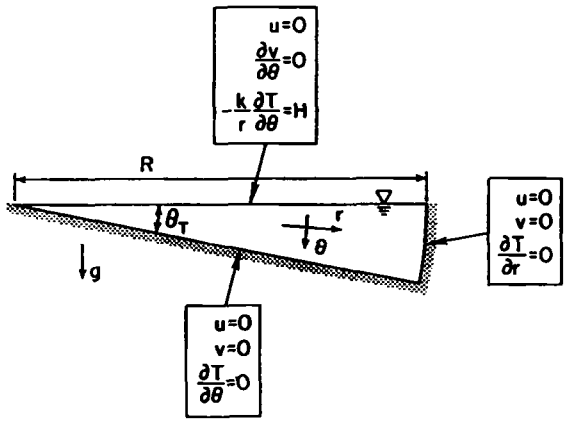

Figure 1. Computational domain and boundary conditions

To make the equations dimensionless, a choice of length, velocity and temperature scales is required. The selection of the pertinent scales in natural convection is a particularly intriguing problem. Detailed scale analysis[6,8] can produce valuable information about the hierarchy of scales, although it is not always easy to substantiate the results and there are examples of incorrect analyses (e.g. those referred to in Reference 8, p. 119). Ultimately, however, if the scales are used solely to make the equations dimensionless for numerical solutions, the selection can be arbitrary at no damage.

A survey of non-dimensionalization scales used in natural convection problems has been given by Ostrach.[4] In the present problem the difficulty in choosing the scales is aggravated, since in addition to the velocity a choice of the temperature scale is also required.

The scales used to normalize the equations for the numerical calculations are

length scale

$$h = R \sin \theta_T, \tag{8}$$

velocity scale

$$v_s = \frac{\nu}{h} gr^{1/2} = \left(\frac{g\beta H}{k}\right)^{1/2} h, \tag{9}$$

time scale

$$t_s = \frac{h^2}{\nu} Gr^{-1/2} = \left(\frac{k}{\beta g H}\right)^{1/2}, \tag{10}$$

temperature scale

$$\Delta T_s = Hh/k, \tag{11}$$

where Gr is the Grashof number. The non-dimensional independent parameters of the problem are

Grashof number

$$Gr = g\beta H h^4/\nu^2 k, \tag{12}$$

Prandtl number

$$Pr = \nu/\alpha, \tag{13}$$

slope of the enclosure

$$S = \tan \theta_T. \tag{14}$$

The Rayleigh number $Ra = Gr\ Pr$ can be used instead of Gr. These scales (equations (9) and (10)) have been used before, e.g. by Moore and Weiss[5] in a numerical study of the confined Bénard problem. They did not prove particularly useful here, since use of α/h and h^2/α as velocity and time scales respectively would have made explicit the insensitivity of the flow to Pr as discussed later. (The numerical results would of course have been identical.) The thermal diffusivity $\alpha = k/\rho c$.

2.2. *Quasi-steady convection problem*

Because the domain is cooled from the surface while the bottom and the side are insulated, the water temperatures will keep dropping and no steady state in terms of temperatures can be reached. Because the fluid properties (ν, α, k) are represented as constants and the density is expressed as a linear function of temperature, a state can be reached, however, where the velocities and the temperature gradients (instead of the temperature) become steady. In this state, which is referred to as a quasi-steady state, the temperature drops at the same rate everywhere:

$$\frac{dT_q}{dt} = -\frac{2H}{\rho c R \theta_T}, \tag{15}$$

where c is the specific heat, or in dimensionless form with $\phi = (T_0 - T)\Delta T_s$

$$\frac{d\phi_q}{dt} = 2Ra^{-1/2}Pr^{-1/2}\frac{\sin\theta_T}{\theta_T}. \tag{16}$$

Thus we have split the temperature into two components: a spatially averaged temperature which decreases linearly in time (the solution of equation (15)) and a component which, after the initial transient, settles into a steady state spatial distribution.

Substituting $T(r, \theta, t) = -2Ht/\rho c R\theta_T + \tau(r, \theta, t)$ into equation (4) gives

$$\frac{\partial\tau}{\partial t} + v\frac{\partial\tau}{\partial r} + \frac{u}{r}\frac{\partial\tau}{\partial\theta} = \alpha\left[\frac{1}{r}\frac{\partial}{\partial r}\left(r\frac{\partial\tau}{\partial r}\right) + \frac{1}{r^2}\frac{\partial^2\tau}{\partial\theta^2}\right] + \frac{2H}{\rho c R\theta_T}. \tag{17}$$

Since all boundary conditions for T involve gradients only and are independent of time, the same boundary conditions apply for τ as for T.

The model consisting of equations (1)–(3) and (17) and boundary conditions (5)–(7) is equivalent to the original model and can be interpreted as the model of an enclosure with a uniformly distributed heat source equal to $2H/\rho c R\theta_T$; the enclosure is being cooled from the surface. Since τ can reach a steady state, no distinction is necessary between the quasi-steady state for temperature T and the steady state for τ. Computationally, however, it is more efficient to solve the problem consisting of equations (1)–(3) and (17), especially for high Ra where the flow becomes time-dependent. In the following, T will be substituted for τ while referring to equation (17).

2.3. *The steady conduction problem*

Among the quantities to be extracted from the numerical solutions in terms of velocity components $u(r, \theta)$ and $v(r, \theta)$ and temperature $T(r, \theta)$ are the strength of the circulation or volumetric flow rate Q and the total radial heat transfer $\bar{H}$, which are defined as

$$Q(r) = \tfrac{1}{2}\int_{\theta=0}^{\theta_T} |v(r, \theta)| r\, d\theta, \tag{18}$$

$$\bar{H}(r) = \int_{\theta=0}^{\theta_T}\left(\rho c T v - k\frac{\partial T}{\partial r}\right) r\, d\theta. \tag{19}$$

These are made dimensionless as

$$Q' = Q/v_s h, \qquad \bar{H}' = \bar{H}/Hh \tag{20}$$

The steady state of $\bar{H}$ can be found by integrating equation (17) over the angular direction (this will be subsequently referred to as 'depth integration'). The result is

$$\bar{H}(r, t) = Hr\left(\frac{r}{R} - 1\right) - \int_{r=0}^{R} \int_{\theta=0}^{\theta_T} \rho c \frac{\partial T}{\partial t} r \, d\theta \, dr. \tag{21}$$

At steady state

$$\bar{H}_{st}(r) = Hr\left(\frac{r}{R} - 1\right) \tag{22}$$

or in dimensionless form

$$\bar{H}_{st}(r') = r'(r' \sin \theta_T - 1). \tag{23}$$

Equation (22) shows that the steady horizontal heat transfer is of course determined solely by the geometry of the domain and the temperature boundary conditions and not by the medium in which the transfer takes place. It is therefore instructive to examine the solution of the temperature field which develops in a solid domain (pure conduction problem) subjected to the same temperature boundary conditions. The solution is most readily obtained in Cartesian co-ordinates.

For a pure conduction problem the energy equation that corresponds to equation (17) is

$$k\left(\frac{\partial^2 T}{\partial x^2} + \frac{\partial^2 T}{\partial y^2}\right) + \frac{2H}{h} = 0, \tag{24}$$

with boundary conditions

$$k \left.\frac{\partial T}{\partial y}\right|_{y=0} = H, \qquad \left.\frac{\partial T}{\partial y}\right|_{y=Sx} = S \left.\frac{\partial T}{\partial x}\right|_{y=Sx}, \qquad \left.\frac{\partial T}{\partial x}\right|_{x=l} = 0, \tag{25}$$

where $S = h/l$ and h and l are as indicated in Figure 2.

The solution is

$$T(x, y) = \frac{Hh}{k} S^{-2}\left\{\frac{x}{l} - \frac{1}{2}\left(\frac{x}{l}\right)^2 + S^2\left[\frac{y}{h} - \frac{1}{2}\left(\frac{y}{h}\right)^2\right]\right\}. \tag{26}$$

The isotherms corresponding to this solution can be seen in Figure 3.

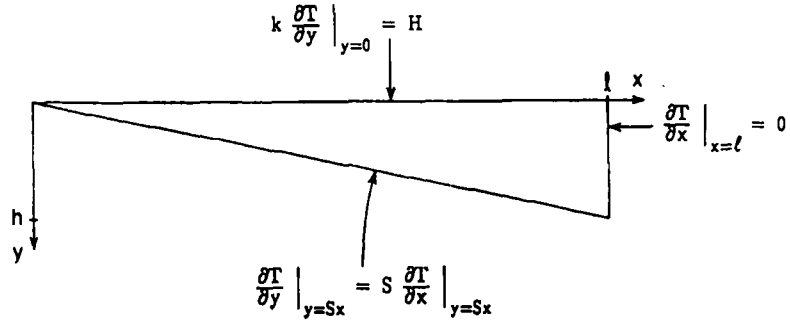

Figure 2. Domain and boundary conditions for the conduction problem in Cartesian co-ordinates

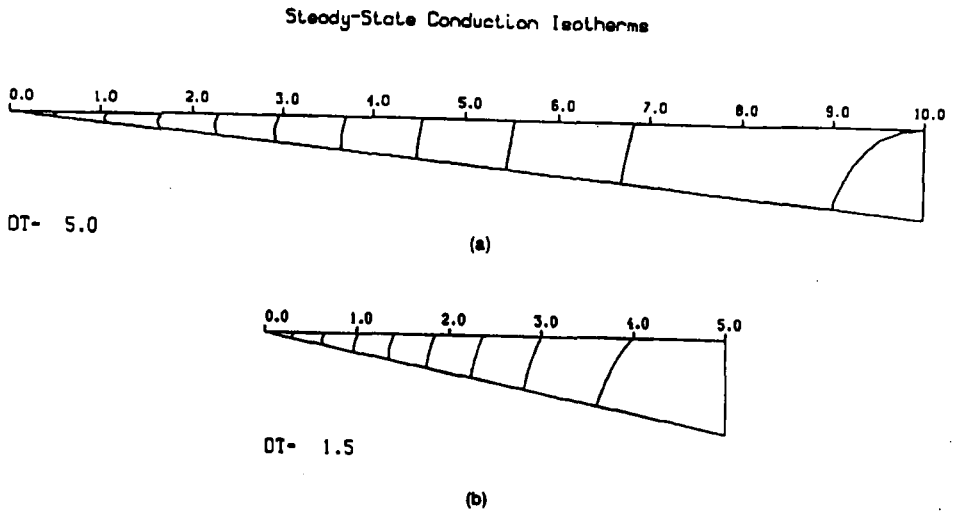

Figure 3. Steady state isotherms for pure conduction (equation (26)) for (a) $S = 0{\cdot}1$ and (b) $S = 0{\cdot}2$

Taking $\Delta T_x = T(l, 0) - T(0, 0)$ as a measure of the horizontal temperature difference, we find

$$\Delta T_x = \frac{1}{2}\frac{Hh}{k} S^{-2}. \tag{27}$$

Since, as already mentioned, the steady horizontal heat transfer is imposed by the geometry and boundary conditions, the ratio of ΔT_x which develops in a fluid flow divided by the value for conduction (equation (27)) can be taken as an indication of the relative importance of convective versus conductive transfer. Equation (27) shows that the pertinent horizontal temperature scale for the conduction problem is

$$\Delta T_x \sim \frac{Hh}{k} S^{-2}. \tag{28}$$

In Reference 9 the scale of equation (28) rather than the scale Hh/k is shown to be the pertinent horizontal temperature scale for a more general class of slopes by examining asymptotic solutions as $S \to 0$.

2.4. Numerical method

The equations for the flow problem were solved numerically using the SIMPLE algorithm of Patankar and Spalding.[10] The details of the method described in Reference 11 have been implemented in the code of Reference 12. The main features of the method and some modifications of the original code are summarized below.

The method arrives at a solution of the coupled, non-linear system of the equations of momentum, continuity and energy through successive iterations. During each iteration a linearized form of each component of the momentum equation (u, v) is solved, followed by a pressure correction equation (p'), which has been derived from the continuity equation, and the energy equation (T). The matrix that results during the solution of each of these problems, (u, v, p', T), is solved by a line-by-line method utilizing the tridiagonal matrix algorithm.

The discretization of the differential equations is based on a finite volume formulation which preserves the conservation properties of the equations exactly in the control volume that surrounds each grid point, for coarse and fine grids alike. The convection–diffusion terms are interpolated using the power-law scheme of Reference 13, which is a computationally efficient, close approximation of the exponential scheme. The properties of these schemes were useful in this study, where, at least for small Ra, the grid Peclet (Pe) number was found to range from small to large values in different parts of the computational domain. The remaining terms, e.g. the additional terms due to polar co-ordinates, were discretized separately. The grid is staggered, i.e. the two components of the velocity and the pressure are calculated at different locations to avoid the development of spurious pressure waves. The time marching is fully implicit even though, because of the possibility of the development of physical (convective) instability, the time step was small enough to satisfy a Courant criterion.

Two modifications were implemented in the original code. The first aimed at making possible unsteady solutions by allowing iterations within a time step. The second aimed at improving the efficiency of the code on a vector processor.

3. RESULTS OF THE NUMERICAL SOLUTIONS

3.1. *Range of independent variables*

To gain insight to the development and steady state of the flow model consisting of equations (1)–(4) and boundary conditions (5)–(7), also depicted in Figure 1, numerical solutions were calculated for different values of the independent parameters Ra, Pr and S. Since the time required for the flow to develop is among the dependent variables of interest, the solutions were initiated from a quiescent and isothermal initial condition. The calculated parameters chosen to characterize the dependence of the solutions on the independent parameters of the problem at steady state are $u_{r_{max}}$, Q_{max} and $\Delta T_{r_{max}}$ at $\theta = \theta_T$. To make the interpretation of the solutions described below unambiguous, a summary of the variables of the problem together with the scales used to normalize them is given in Table I. Solutions were calculated for selected triplets of $Ra = 10^4$,

Table I. Summary of independent and dependent variables, reference quantities and their scales

	Name and symbol	Non-dimensionalization scale	Non-dimensional variables
Independent variables	Radial co-ordinate r	$h = R \sin \theta_T$ (equation (8))	$r' = r/h$
	Angular co-ordinate $r\theta$	h as above	
	Time t	$t_s = h^2 Gr^{-1/2}/\nu$ (equation (10))	$t' = t\nu Gr^{1/2}/h^2$
Dependent variables	Radial velocity u	$v_s = \nu Gr^{1/2}/h$ (equation 9)	$u' = uhGr^{-1/2}/\nu$
	Angular velocity v	v_s as above	$v' = vhGr^{-1/2}/\nu$
	Temperature T	$\Delta T_s = H\,h/k$ (equation (11))	$t' = Tk/Hh$
Point reference quantities	Maximum radial velocity $u_{r_{max}}$	v_s as above	$u'_{r_{max}} = u_{r_{max}}/v_s$
	Maximum temperature difference $\Delta T_{r_{max}}$	ΔT_s as above	$T' = T/\Delta T_s$
Integral reference quantity	Maximum flow rate Q_{max} (equation (18))	$v_s h = \nu Gr^{1/2}$ (equation (20))	$Q' = Q/v_s h$

10^6, 10^8, $Pr = 7$, 10^2, 10^3 and $S = 0{\cdot}2, 0{\cdot}1$. Because the stability characteristics of the flow depend on Ra, a different regime results for each of the Ra-values. The main features of these results remain unaffected by Pr and, to a lesser degree, by changes in S within the examined ranges. It is therefore convenient to describe the flow for each value of Ra, followed by observations about the Pr influence. The influence of the slope is discussed in Section 3.6.

3.2. Low-Rayleigh-number regime: $Ra = 10^4$

Flow development in time. The development of the flow from its inception at the onset of surface heat loss to the steady state is depicted in Figure 4 for $Ra = 10^4$, $Pr = 10^3$ and $S = 0{\cdot}2$. All the quantities shown there have been normalized with the scales presented in Section 2 and summarized in Table I.

The solution is based on 40×25 (r, θ) grid points. Since the length scale used to normalize the equations is h, i.e. the depth of the enclosure, given by equation (8), it follows that the dimensionless depth is 1. The dimensionless radius is $R' = 1/\sin \theta_T$, where θ_i, $i = 1, \ldots, 23$, are the co-ordinates of the control volume faces; $\Delta t = 0{\cdot}25$ for $Pr = 7$, $0{\cdot}5$ for $Pr = 10^2$ and $0{\cdot}5$ for $Pr = 10^3$.

At dimensionless time $t = 50$ the $T = 0$ isotherm is parallel to the surface along almost the entire enclosure (Figure 4); near the region where it meets the sloping boundary, however, it curves so as to meet this adiabatic boundary perpendicularly as required. Thus a local temperature gradient is created which initiates a counterclockwise-rotating cell at the shallow end. This cell in turn initiates through shear a clockwise-rotating cell which extends along the entire deep end of the enclosure. The first important feature of the low-Ra regime is that for $S = 0{\cdot}2$ this deep-end cell remains stable, i.e. it does not break into smaller cells at a later time, so that during the rest of the development of the flow the shallow-end cell grows at the expense of the deep-end cell until the latter disappears. The second important feature of this regime is that a steady state is eventually reached (i.e. u, v, T and p become time-independent).

Because the $T = 0$ isotherm is parallel to the surface (Figure 4), it can be inferred that at this time instant the flow does not contribute to the heat transfer, which is predominantly conductive. This is corroborated by the calculated horizontal heat flux also plotted in Figure 4. The total heat transfer is separated into its conductive and advective components and the latter is zero. (Caution, however, must be exercised in interpreting this graph because of possible cancellation effects of this two-layer flow.) At a later stage, e.g. $t = 800$ in Figure 4, the isotherms and the heat transfer graph indicate the beginning of interaction of the flow with the heat transfer. The third set of graphs in Figure 4 is for time $t = 2300$ and depicts the stage where the deep-end cell has been suppressed. Finally, at time $t = 5250$ Figure 4 shows the quasi-steady state. At steady state the flow consists of one elongated cell which can be viewed as a two-layer flow in its middle part. The evolution into a quasi-steady flow field is also illustrated in the plot of horizontal (radial) velocities versus time at selected points (Figure 5).

Dependence on Prandtl number Pr. A very interesting feature of the flow is its lack of dependence on the Prandtl number Pr when $Pr > 7$ (which corresponds e.g. to water at 20 °C). The numerical calculations show that the velocities which have been made dimensionless by the velocity scale given in equation (9) increase proportionally to $Pr^{-1/2}$. It follows that if the velocities are made dimensionless by α/h, they will be independent of Pr. This holds true for the entire period of development as well as for the quasi-steady state. Actually, it can be seen that for the values reported in Table II, the velocity maximum $u_{r_{max}}$ (scaled by α/h, i.e. $u_{r_{max}} h_s/\alpha$) for $Ra = 10^4$ and $Pr = 7$ is within 0·5% of the maxima for $Pr = 10^2$ and $Pr = 10^3$. Since the scaled

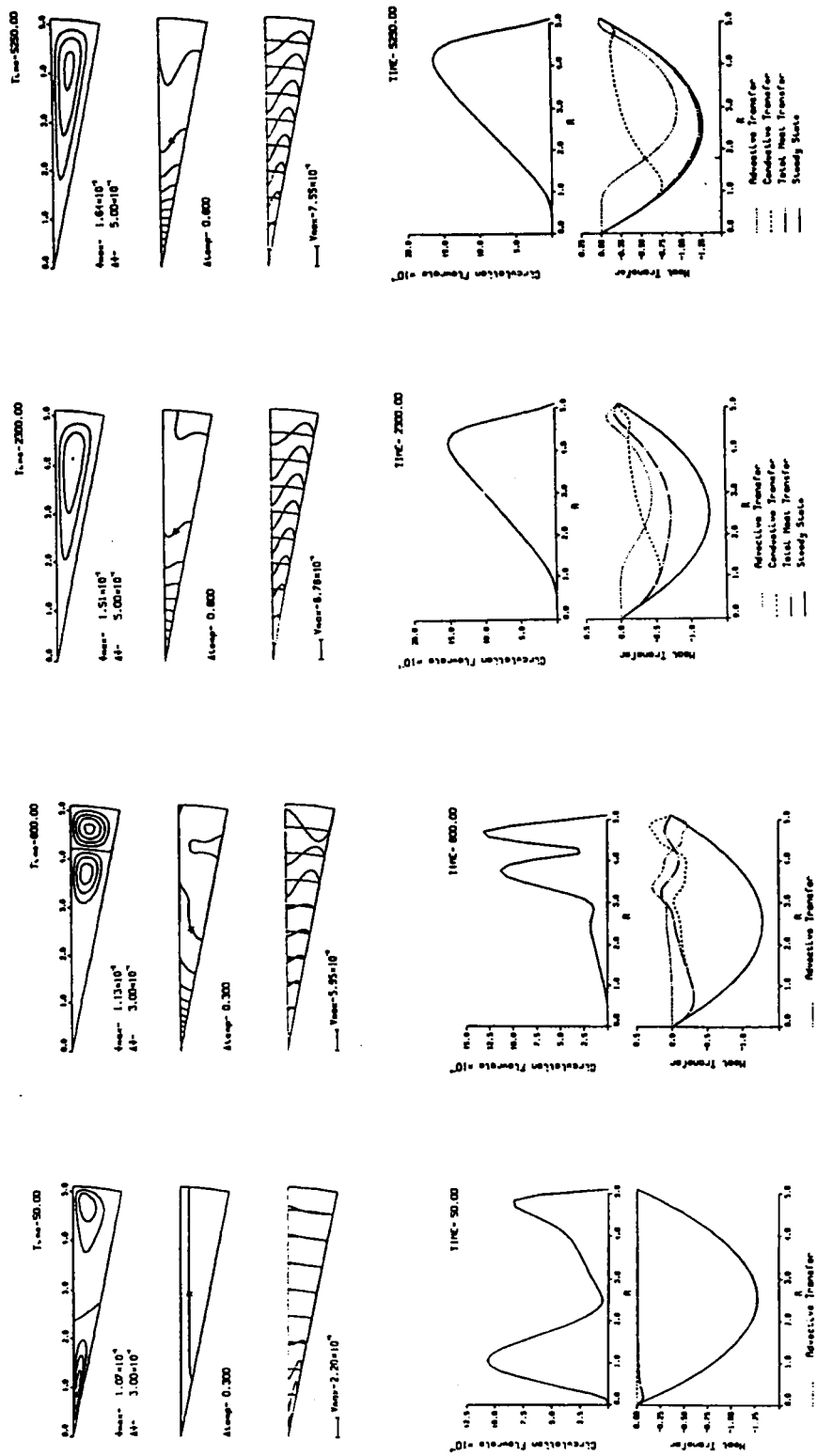

Figure 4. Evolution of the flow for $Ra = 10^4$, $Pr = 10^3$, $S = 0{\cdot}2$. From top to bottom the instantaneous graphs represent (i) streamlines, (ii) isotherms (the asterisk marks the $T = 0$ isotherm), (iii) radial velocity profiles, (iv) horizontal circulation (equation (18)) and (v) horizontal heat transfer (equation (19))

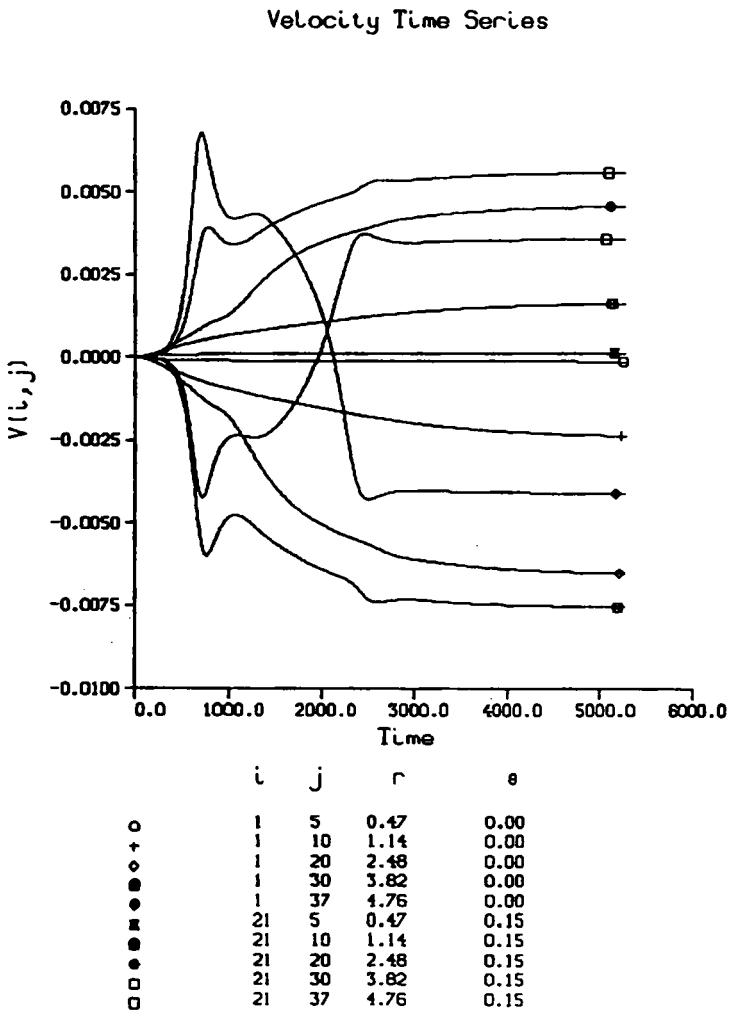

Figure 5. Radial velocity (u_r) time series at selected points for $Ra = 10^4$, $Pr = 10^3$, $S = 0{\cdot}2$

velocity fields are identical for different Pr-values, the same applies for the flow rates Q (equation (8) and Table III).

The important implication of this property of the flow is that the non-linear advective terms of the momentum equations are negligible. Effectively, then, the non-linearities of this problem come from the advective terms of the energy equation and from the coupling through buoyancy of the momentum and energy equations.

The Pr-independence of the appropriately scaled flow quantities is not a feature unique to the particular flow examined herein. In fact, as is well documented in the heat transfer literature, it seems to be common among natural convection flows in enclosures. For example, De Vahl Davis[14] and Quon[15] found that the steady, two-dimensional solutions of the flow in a square enclosure with differentially heated vertical walls are largely independent of Pr for Ra-values up to about 10^6. Mallinson and De Vahl Davis[16] confirmed that this property of the flow also holds for three-dimensional solutions. These studies concluded that at $Pr = 7$ the flow

Table II. Radial velocity maxima ($u_{r_{max}}$) at steady state for different *Ra*- and *Pr*-values; *x* is the exponent in $u_{r_{max}} = APr^x$

Pr	$Ra = 10^4$	10^6	10^8
7	$9{\cdot}01 \times 10^{-2}$	$6{\cdot}45 \times 10^{-2}$	$4{\cdot}10 \times 10^{-2}$
10^2	$2{\cdot}39 \times 10^{-2}$	$1{\cdot}78 \times 10^{-2}$	$1{\cdot}12 \times 10^{-2}$
10^3	$7{\cdot}55 \times 10^{-3}$		
x	−0·50	−0·49	−0·49

Table III. Radial flow rate maxima (Q_{max}) at steady state for different *Ra*- and *Pr*-values

Pr	$Ra = 10^4$	10^6	10^8
7	$1{\cdot}96 \times 10^{-2}$	$1{\cdot}11 \times 10^{-2}$	$6{\cdot}85 \times 10^{-3}$
10^2	$5{\cdot}20 \times 10^{-3}$	$3{\cdot}00 \times 10^{-3}$	$1{\cdot}85 \times 10^{-3}$
10^3	$1{\cdot}64 \times 10^{-3}$		

behaves as for infinite *Pr*, while the difference at $Pr = 1$ is surprisingly small (of the order of a few per cent).

Moore and Weiss[5] studied the Rayleigh–Bénard problem by extracting two-dimensional numerical solutions. They found that for *Pr*-values greater than unity the Nusselt number *Nu* is independent of *Pr* (termed the viscous regime). Also, the velocity scale they gave for this regime, i.e. $w \sim Ra^{2/3}\alpha/h$, is independent of *Pr*. The domain of validity of the viscous regime was found, however, to depend on the relative *Ra*- and *Pr*-values. Busse[17] cites further evidence that for the Bénard problem *Nu* is independent of *Pr* when $Pr > 1$; in this regime the stability properties of convection depend on the non-linearities of the heat equation.

Accuracy of the solutions. To appraise the accuracy of the calculations, solutions obtained on two different (r, θ) grids, one 30 × 15 and the other 40 × 25, for $Ra = 10^4$, $Pr = 7$ and $S = 0{\cdot}2$ were compared. The grid was non-uniform in the θ-direction, being progressively thinner towards the surface. The overall evolution of the flow was qualitatively identical for the two different resolutions, with the boundary between the two cells (Figure 6) being at nearly the same position. As for any fixed grid calculation of a flow that exhibits transient formation and disappearance of cells, however, the calculation becomes less accurate when the extent of the disappearing cell becomes comparable with the spatial resolution. Thus before $t = 35$ the maximum radial velocity $u_{r_{max}}$ of the two solutions was within 5%, whereas between $t = 35$ and 70 the difference was close to 20%, with the maximum difference (25%) occurring at $t = 47{\cdot}5$ (see Figure 6). Shortly before the disappearance of the deep-end cell, however, and up to the steady state the difference in $u_{r_{max}}$ between the two solutions is less than 0·2%.

The dimensionless time step used to calculate the solutions was 0·25, 0·5, 0·5 for $Pr = 7$, 10^2, 10^3 respectively. It can be verified *a posteriori* that with the grid and time step in use a Courant number criterion is conformed to (although stability is not an issue, since the method is fully implicit). An indirect verification that the time step was adequate comes from the higher-*Pr* solutions. The time step expressed in h_s^2/α time units (in which the solutions are virtually identical)

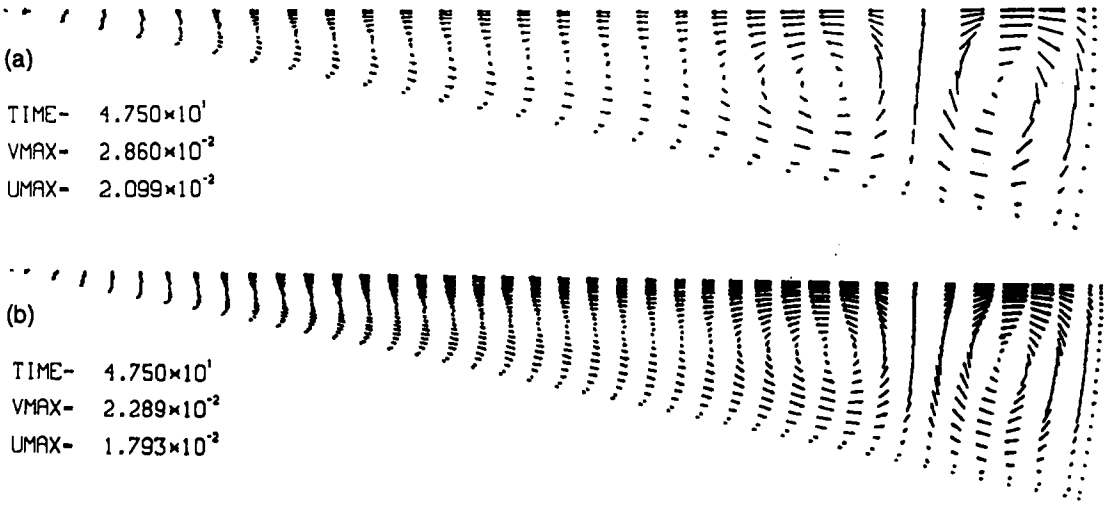

Figure 6. Instantaneous velocity fields at $t - 47{\cdot}5$ for $Ra = 10^4$, $Pr = 7$, $S = 0{\cdot}2$ calculated on 15 × 30 (upper) and 25 × 40 (lower) grids

is $9{\cdot}45 \times 10^{-4}$, 5×10^{-4}, $1{\cdot}58 \times 10^{-4}$ for $Pr = 7$, 10^2, 10^3 respectively. Since decreasing the time step by a factor of six did not produce any differences, the original time step could be considered adequate.

3.3. *Intermediate-Rayleigh-number regime: $Ra = 10^6$*

Flow development in time. A sequence of streamline, isotherm and radial velocity plots depicting the evolution of the flow at $Ra = 10^6$, $Pr = 7$ and $S = 0{\cdot}1$ appears in Figure 7. The solution is based on 30 × 80 (θ, r) grid points. The domain dimensions are as for the $Ra = 10^4$ solution. For this run $\Delta r' = 0{\cdot}0654$; $\theta_i = [(i - 1)/28]^{**}1{\cdot}5/\theta_T$, where θ_i, $i = 1, \ldots, 28$, are the co-ordinates of the control volume faces; $\Delta t = 0{\cdot}25$ for $Pr = 7$ and $0{\cdot}5$ for $Pr = 10^2$. The description of the main features of the flow is generic and applies also for $Pr = 10^2$ and for $S = 0{\cdot}2$. Further details can be found in Reference 18.

The inception of the flow (Figure 7, $t = 25$) is quite similar to the inception at $Ra = 10^4$ described above. The first distinctive feature of this regime is shown in Figure 7 at $t = 75$, where it can be seen that the deep-end elongated cell breaks into smaller cells. Unlike the shallow-end cell, which is driven by the local, corner temperature gradient, the deep-end cells are the result of physical instability, i.e. they are the equivalent of Bénard cells. It can be recalled that at $Ra = 10^4$ no such cells appeared. The second distinctive feature of the $Ra = 10^6$ regime is that just as for the $Ra = 10^4$ case a steady state is eventually reached (Figure 7, $t = 1250$). This state consists of an elongated cell extending along the entire enclosure, with a secondary cell forming near the surface at the deep end. It is noteworthy that the single-cell regime is reached relatively early in the evolution of the flow (around $t = 400$, Figure 7), whereas the steady state is reached at a much later time (around $t = 1000$). This can be observed more clearly in Figure 8, where time series of the radial velocity at selected points are plotted. After the initial development of the flow the steady state is reached through oscillations and minor adjustments of the flow. For total flow rate and total radial heat transfer it can be seen from Figure 9 that these minor adjustments are important in reaching the steady, horizontal heat transfer.

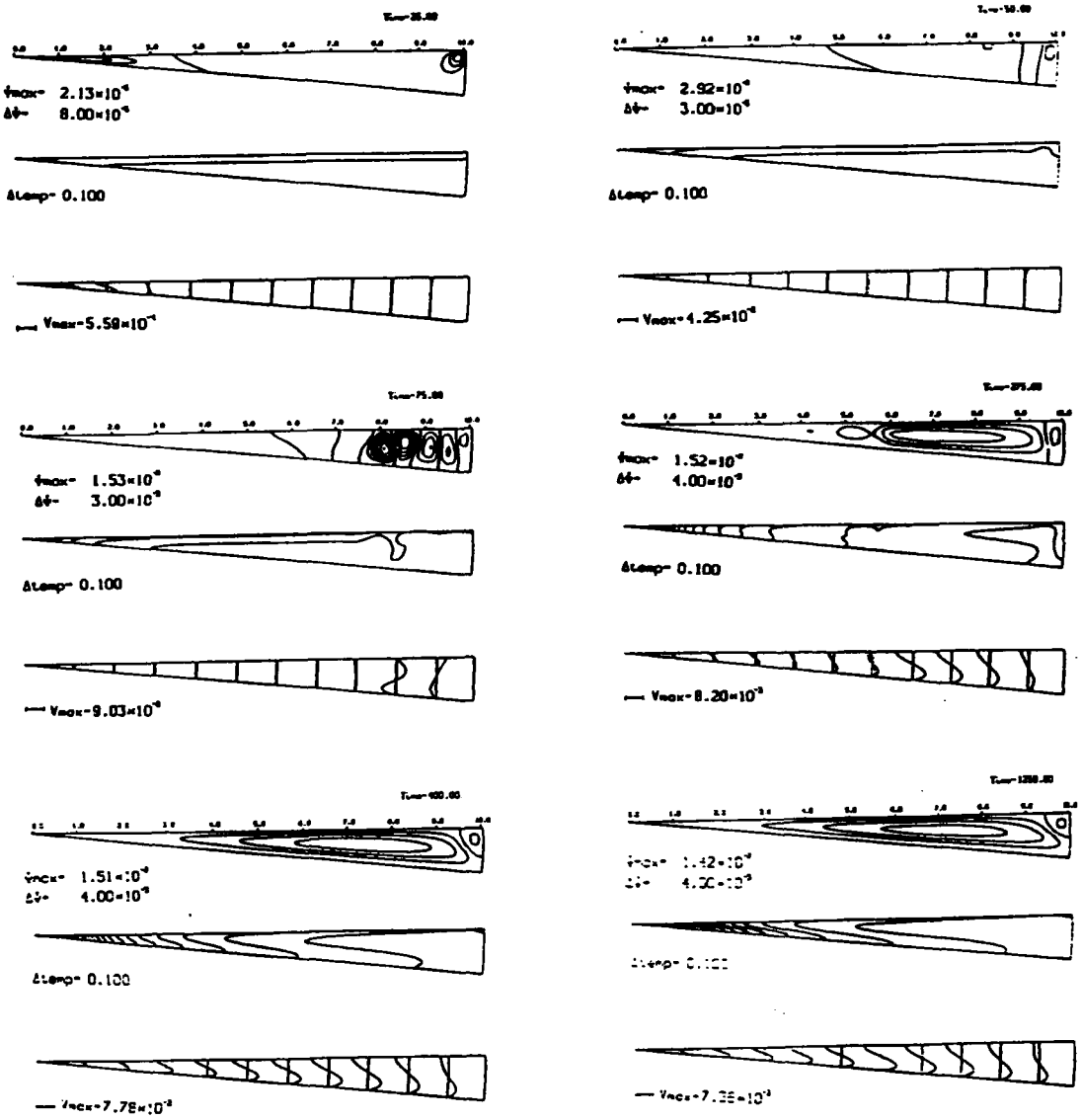

Figure 7. Characteristic stages during the evolution of the $Ra = 10^6$, $Pr = 7$, $S = 0{\cdot}1$ flow on a 30 × 80 grid. At each time instant plots of (from top to bottom) streamlines, isotherms and radial velocity profiles are included

The foregoing observation of the flow development raises a serious question. If several intermittent cells form, interact with each other and finally merge into a single cell, is it possible that the flow will be three- rather than two-dimensional? This situation is to be contrasted with the $Ra = 10^4$ calculation, where the smooth progression from two cells to a single cell makes it likely that the cells could be two-dimensional rolls. The more important question in the $Ra = 10^6$ case is whether the single main cell at steady state results because of the restriction of the flow in two dimensions. Carrying out three-dimensional calculations to settle these questions was precluded by the impractical highly cost of their computation.

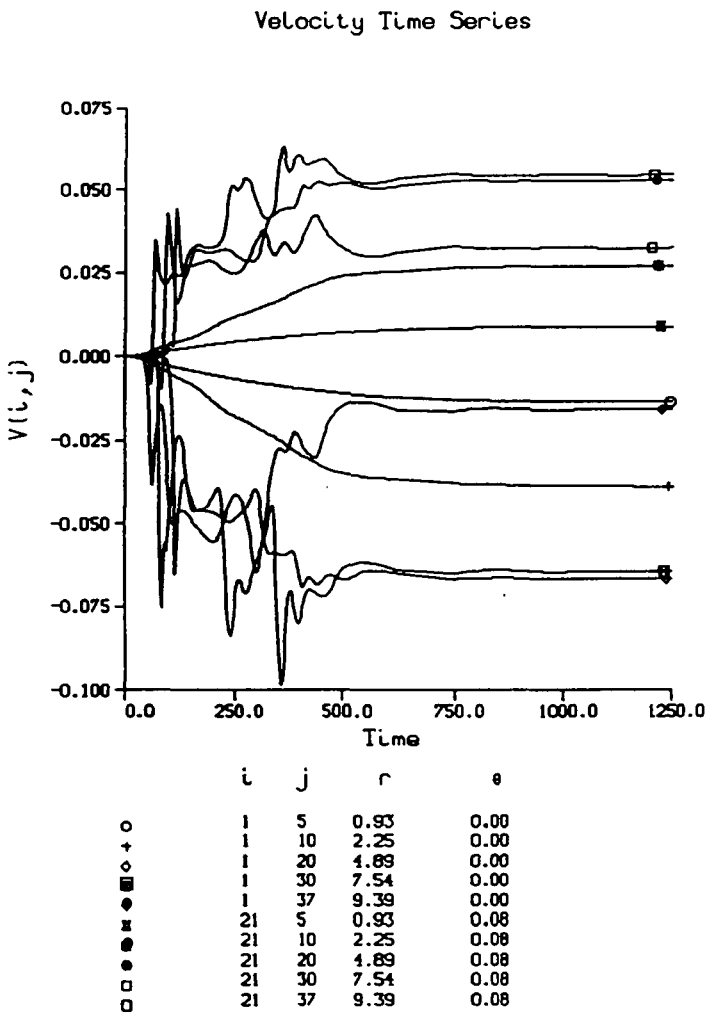

Figure 8. Radial velocity (u_r) time series at selected points for $Ra = 10^6$, $Pr = 7$, $S = 0{\cdot}1$

Dependence on Prandtl number Pr. The role of Pr in the solution at $Ra = 10^6$ is less clear than it is at $Ra = 10^4$, mainly because the unsteady part of the solution is less accurate. At steady state it can be seen that by rescaling the values given in Table I by α/h, the maximum of the velocity at $Ra = 10^6$ is 17·1, 17·8 for $Pr = 7$, 10^2 respectively. Unlike the $Ra = 10^4$ solution, however, the early stages of the evolution are different for each Pr-value, with more vigorous cell velocities appearing at $Pr = 10^2$. Since it is rather unlikely that an increase in Pr should have such an effect, it is more reasonable to attribute these differences to the different time step sizes of the solutions, which were $9{\cdot}45 \times 10^{-5}$ and 5×10^{-5} for $Pr = 7$ and 10^2 respectively. Nevertheless, the development stages parallel each other reasonably closely and it is clear that although the accuracy of the solutions would be improved with finer spatial resolution and a finer time-step, the overall features of development would not change, as explained next.

Accuracy of the solutions. The accuracy of the original 25×40, $Ra = 10^6$, $Pr = 7$, $S = 0{\cdot}1$ solution was examined by making an additional run on a 30×80 grid. At steady state the

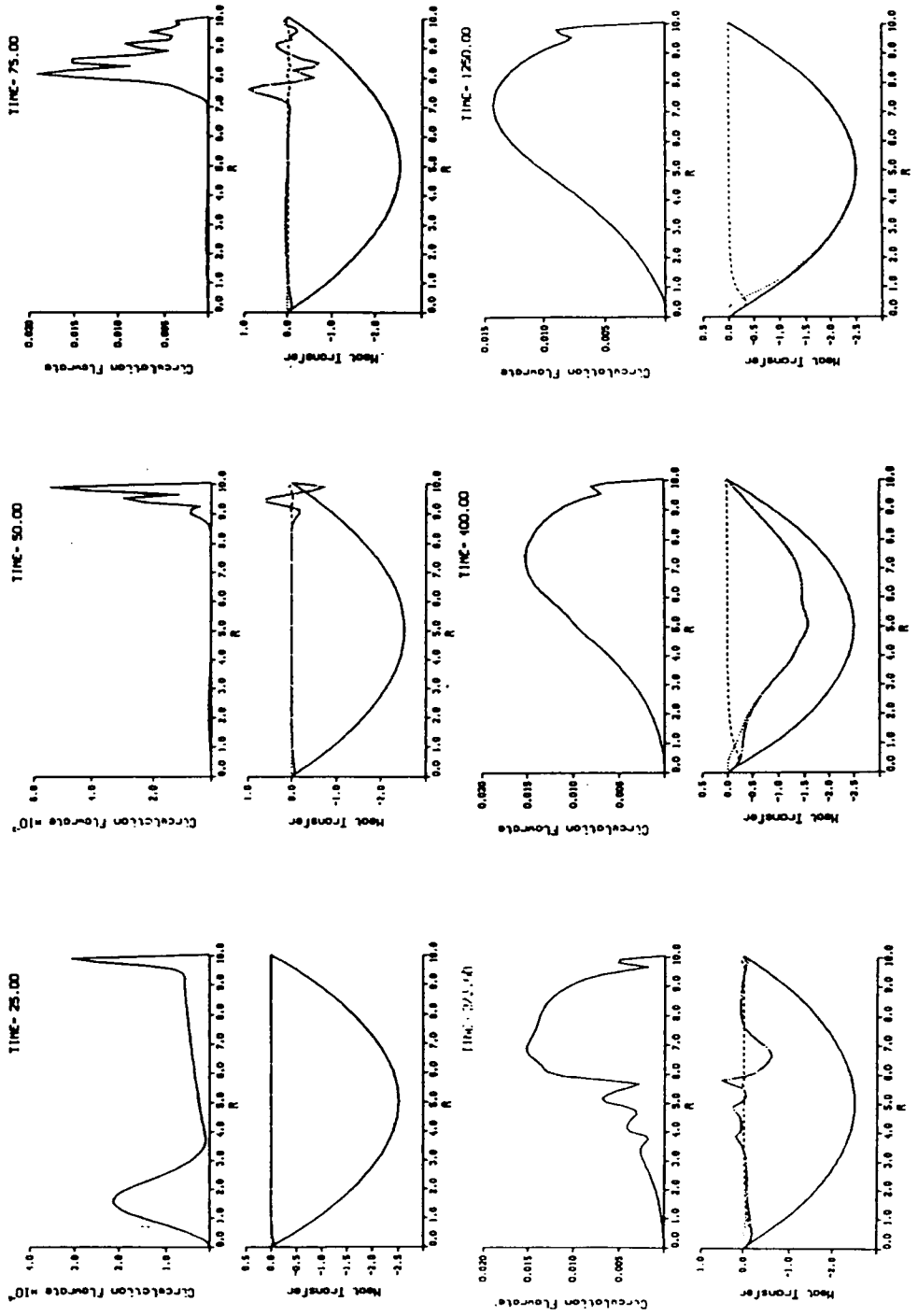

Figure 9. Horizontal volumetric flow rate (equation (18)) and heat transfer rate (equation (19)) for each of the time instants depicted in Figure 7

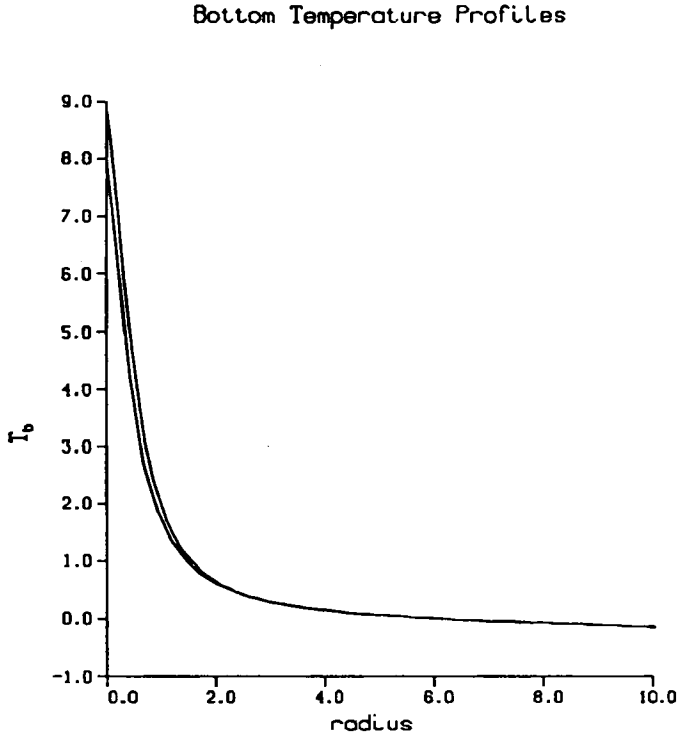

Figure 10. Bottom temperature profiles for $Ra = 10^6$, $Pr = 7$, $S = 0{\cdot}1$ on 30×80 (upper curve) and 25×40 (lower curve) grids

difference was 0·95% in terms of $u_{r_{max}}$ and 7% in terms of ψ_{max} (both maxima occur in the deep part of the domain); ψ is the streamfunction value. The finer grid solution revealed, however, the inadequacy of the discretization of the coarser grid at the pointed end of the domain, since $\Delta T_b = 8{\cdot}48$ for the 30×80 solution while $\Delta T_b = 6{\cdot}93$ for the 25×40 grid (18% difference). The discrepancy can be seen in Figure 10, which compares the bottom temperature profiles for the two different grids and illustrates the sharp temperature drop near the corner. The two profiles virtually coincide nevertheless beyond $r = 2$. In addition, the flow quantities are within 1% at steady state, indicating that the region near the corner where conduction is dominant does not influence the flow very much. During the initial period of flow development the calculations show that the grid significantly influences both the location and strength of the convection cells. This is seen in Figure 11, where the calculated fields (u, v, t) at $t = 100$ are shown for the two different grids ((a) 30×80, (b) 25×40). The characteristic stages, however, such as the formation of cells and the merging of cells to form one main cell (Figure 7), are closely paralleled in the two grids. For $t < 500$ the difference in $u_{r_{max}}$ is up to 25% and that in ψ_{max} up to 30%. After $t > 500$ the differences drop to 1·5% for ψ_{max} and 1% for $u_{r_{max}}$. The sensitivity of the flow pattern to the grid size is a strong indication of how delicate the flow is. It thus seems pointless to seek a fine grid solution for the initial period, especially since the main interest here is in an estimate of the time scale to steady state and in characteristic velocities. Consequently, it was decided to check the accuracy of the $Ra = 10^6$, $Pr = 7$, $S = 0{\cdot}2$ (higher-slope) solution for the steady state only. To this end, the steady state of the 25×40 grid was

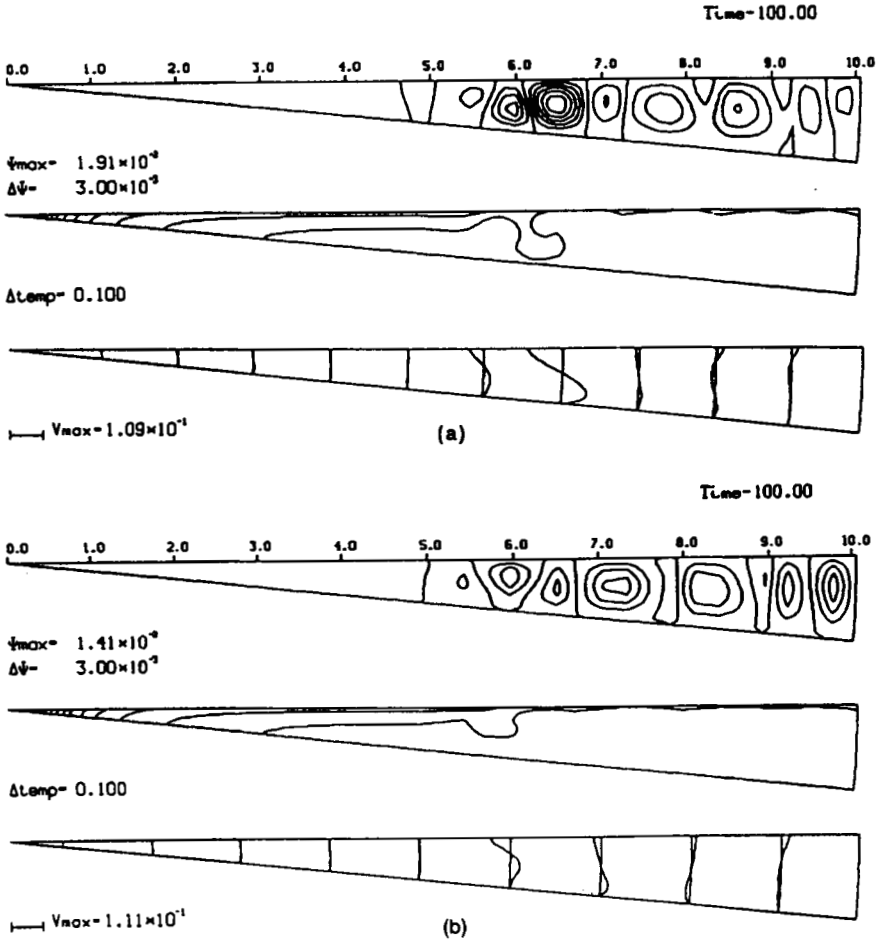

Figure 11. Instantaneous streamlines, isotherms and radial velocity profiles for $Ra = 10^6$, $Pr = 7$, $S = 0{\cdot}1$ on (a) 30 × 80 and (b) 25 × 40 grids

interpolated on a 30 × 80 grid in order to get a close initial guess. This procedure was first tested for the $S = 0{\cdot}1$ slope where the fully unsteady solutions were available on both grids.

By applying this sort of refinement, the solutions at $Ra = 10^6$, $Pr = 7$, $S = 0{\cdot}2$ on 25 × 40 and 30 × 80 grids were found to differ by 0·5% in $u_{r_{max}}$ and less than 0·1% in ψ_{max}.

The effect of the time step on the accuracy of the solution has been discussed in the subsection on Prandtl number effects.

3.4. High-Rayleigh-number regime: $Ra = 10^8$

Flow development in time. The initial development of the flow at $Ra = 10^8$, $Pr = 7$, $S = 0{\cdot}2$ from isothermal and quiescent initial conditions is similar to the already described initiation of flow at $Ra = 10^6$. The $Ra = 10^8$ solution is based on 30 × 80 (θ, r) grid points. The domain dimensions are as for the $Ra = 10^4$ solution. For this run $\Delta r' = 0{\cdot}0654$; $\theta_i = [(i-1)/28]^{**}1{\cdot}5/\theta_T$, where θ_i, $i = 1, \ldots, 28$, are the co-ordinates of the control volume faces; $\Delta t = 0{\cdot}25$ for $Pr = 7$. The important difference between these two flows is that the one-main-cell configuration which

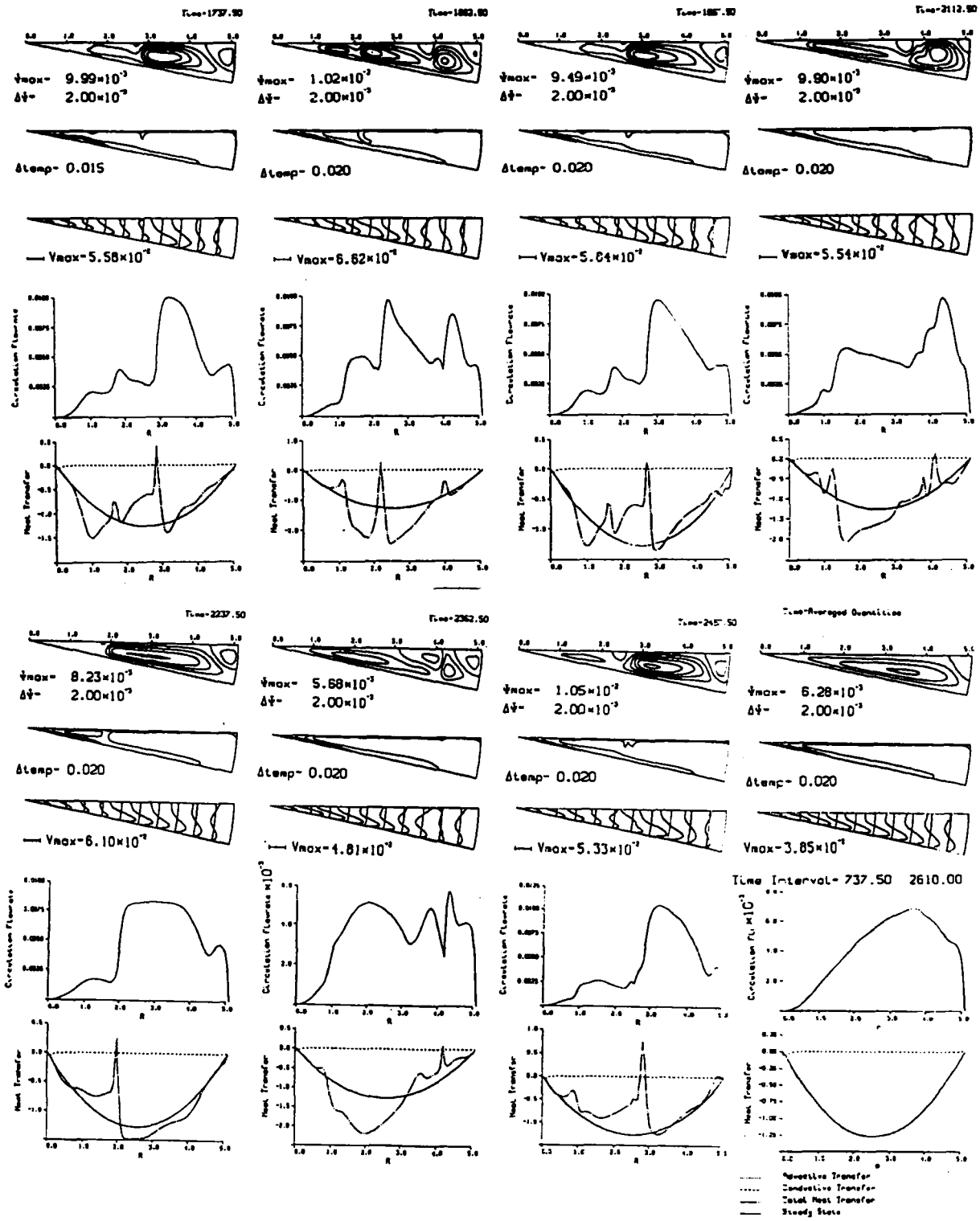

Figure 12. Time instants in the evolution of the $Ra = 10^8$, $Pr = 7$, $S = 0{\cdot}2$ flow. Included at each instant are (from top to bottom) streamlines, isotherms, radial velocity profiles, horizontal flow rate and horizontal heat transfer

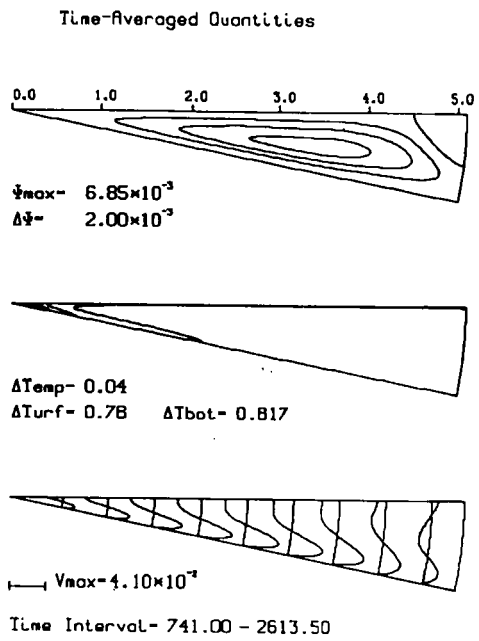

Figure 13. Streamlines, isotherms and radial velocity profiles (from top to bottom) resulting from averaging within the developed time-dependent state of $Ra = 10^8$, $Pr = 7$, $S = 0{\cdot}2$ on a 60×120 grid

represents a steady state at $Ra = 10^6$ is no longer stable at $Ra = 10^8$. This is expected for flows of sufficiently high Ra-values, such as those developing in natural systems or even those observed in the laboratory (see Reference 9 for experiments at $Ra \sim 10^{10}$). The range around $Ra = 10^8$ is also where the thermal boundary layer that forms at the surface of a fluid layer cooled from above becomes intermittent (i.e. time-dependent).[19] The recurrent formation and disappearance of ephemeral secondary cells that disrupt the horizontal flow to varying degrees is depicted in Figure 12. In this figure the temperature in the bulk of the domain is remarkably uniform compared with the sharp temperature drop at the shallow corner. This feature has been also observed experimentally (see Reference 9, pp. 71 and 88).

The time-averaged streamlines and isotherms are shown in Figure 13. These quantities have been averaged over a time interval that excludes the initial development. The criterion for the adequacy of the averaging interval was based on the closeness of the time-averaged, 'depth'-integrated (i.e. integrated over the angular direction) heat transfer rate to the steady state values of this quantity (equation (23)). This criterion is arbitrary insofar as the degree of closeness of the two curves is arbitrary; it was found that different degrees of proximity resulted in differences of a few per cent in mean values of $Q_{\max}$ and $v_{r_{\max}}$. For the time interval $t = 741$ to 2613 chosen for the mean plots of Figure 13, the time-averaged, depth-integrated flow rate and heat transfer appear in Figure 14, where it can be seen that the time-averaged heat transfer rate visually coincides with its steady state space distribution. The standard deviations of the computed Q and $\bar{H}$ time series normalized by the local mean values are presented in Figure 15. The shape of these curves, which initially increase linearly and then abruptly become almost constant, indicates a depth scale beyond which the flow is less dependent upon the local depth.

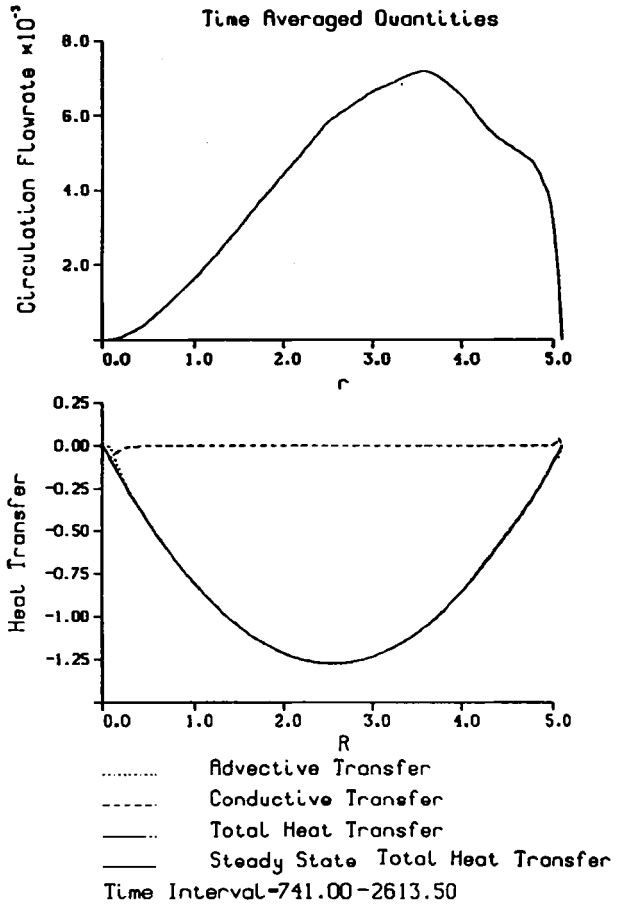

Figure 14. Time-averaged flow rate and horizontal heat transfer corresponding to the fields depicted in Figure 13

Spatial resolution criteria—accuracy. For the numerical solution to be qualitatively correct, the intrinsic length scales of the problem have to be adequately discretized. The horizontal grid size is constrained by the length scale of the developing surface instability and the scale of the convective cells (thermals) that develop past marginal stability, while the vertical resolution is constrained by the thickness of the surface thermal boundary layer. Estimates for each of these were used to make the grid of an $Ra = 10^8$, $S = 0{\cdot}2$ and $0{\cdot}1$, $Pr = 7$ (which represents water at 20 °C) run.

The aforementioned scales were estimated using the numerical and experimental studies of Foster,[20–22] Katsaros *et al.*[23] and Tamai and Asaeda.[24] The details can be found in Reference 3.

Since it is well known (and has already been observed for the $Ra = 10^6$ solution) that in the time-dependent regime the solutions are very sensitive to grid details (see e.g. Reference 25), it is pointless to assess the accuracy of the solutions in terms of instantaneous fields; rather, the dependence of the solution on mesh size is made in terms of time-averaged quantities and the characteristics of fluctuations. It has been noted in the literature that 'statistical results [of coarse grid simulations] are sometimes surprisingly close to those of well resolved turbulent flows'.[26] Numerical solutions of the flow field at $Ra = 10^8$, $Pr = 7$, $S = 0{\cdot}2$ were obtained for two different

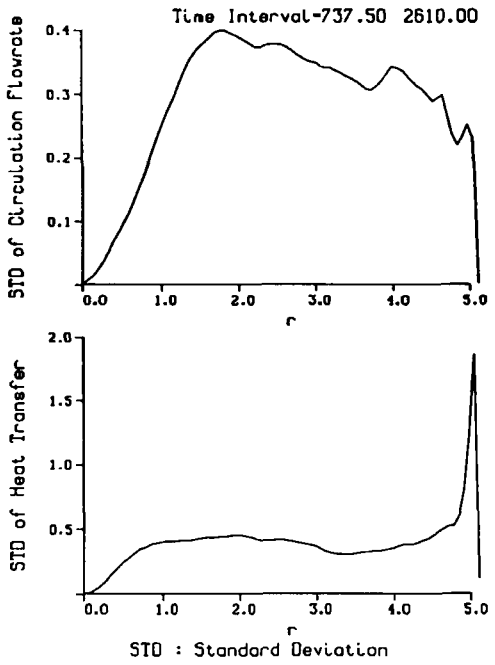

Figure 15. Standard deviations corresponding to the mean fields shown in Figure 14

(θ, r) grid resolutions, namely 30 × 80 and 60 × 120. On the coarser mesh the solutions were started from isothermal and quiescent conditions. After the time interval $t = 741$ to 2600 was found to be adequate for averaging according to the criterion discussed above, the instantaneous fields at $t = 741$ were interpolated on the thinner mesh and a run of equal length was performed. It was found that the fine grid solution satisfied the averaging criterion equally well. In terms of maxima, the two solutions differed by 8·3% in ψ_{max} and 6·1% in $u_{r_{max}}$; the functional form of the ψ- and u-fields is very similar for the two different grids. In terms of the standard deviations of the Q- and $\bar{H}$-values (equation (26)) as reported in Figure 15, the maximum difference between the two calculations was 7%.

3.5. Interpretation of the dependence on Rayleigh number

Having described in the preceding subsections the three flow regimes that correspond to three different Ra-values, it is useful to summarize the results by examining the effects that an increase in Ra has on the flow. The dependence of v_{max}, v_{mean} and Q_{max} on Ra is shown in Figures 16(a) and 16(b). From the description of the flow given in Sections 3.2–3.4, it follows that since the flow configuration (flow pattern) is different for each Ra-value, it is not expected that a single scaling law will fit the velocity and flow rate dependences on Ra, so that Figures 16(a) and 16(b) should be regarded as a mere summary of the results of the numerical experiments.

For a given fluid, e.g. water, an increase in Ra can be interpreted as being due to either an increase in surface heat loss rate H or an increase in maximum depth h (equation (12)). Because of the importance which this distinction has in applications, it is of interest to examine each case separately.

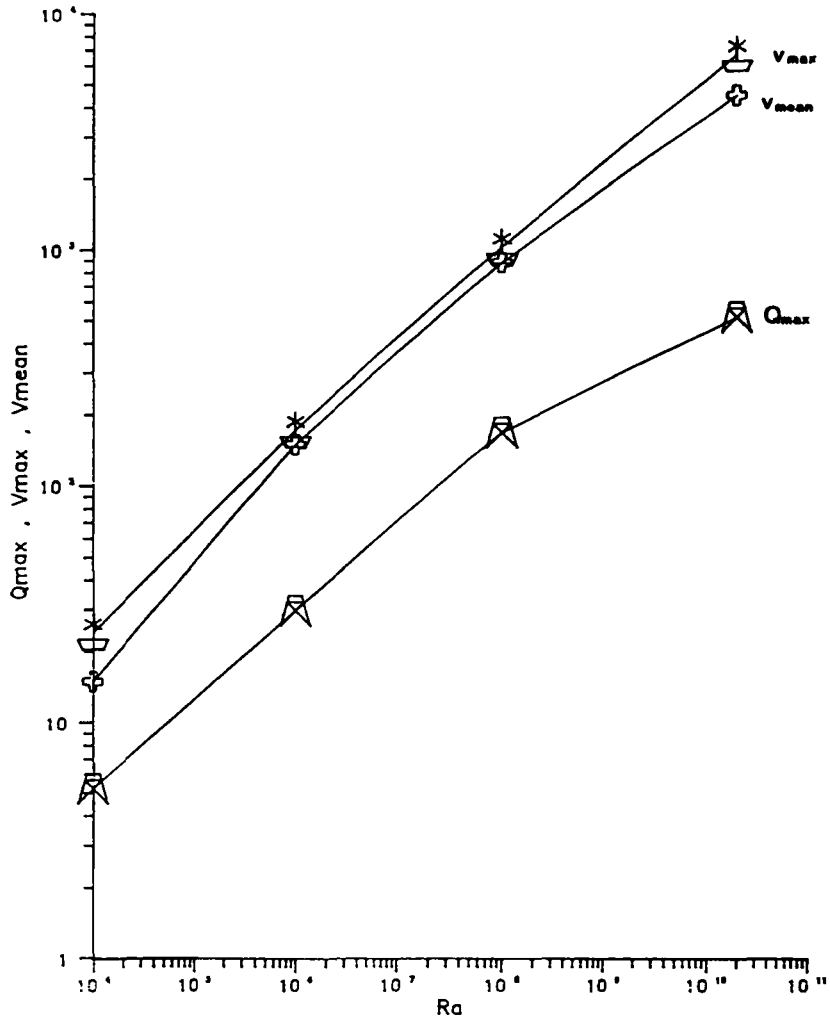

Figure 16(a). Dependence of dimensionless v_{max}, Q_{max} and v_{mean} on Ra for $Pr = 7$, $S = 0{\cdot}2$. The velocities have been normalized using a/h and the flow rate using a. The values corresponding to $Ra = 2 \times 10^{10}$ have been measured experimentally

Effects of increase in depth h. The effect that an increase in depth h has on the flow is of particular interest in examining the relevance of solutions of the numerical model to the analysis of cooling-induced currents in a littoral-like lake domain, where the deep-end boundary is open rather than closed. This is because a domain corresponding to a smaller depth h (i.e. smaller Ra-value) can be considered as being imbedded in a domain of larger h (i.e. larger Ra-value). The flow of the overlapping part in the larger domain is then regarded as the open-ended equivalent of the flow of the small, closed-end domain. The relative size of domains corresponding to $Ra = 10^4$, 10^6, 10^8 is $1/10{:}1/\sqrt{10}{:}1$. The effects of the deep-end boundary are assessed by comparing the horizontal (radial) circulation flow rate curves in the two domains.

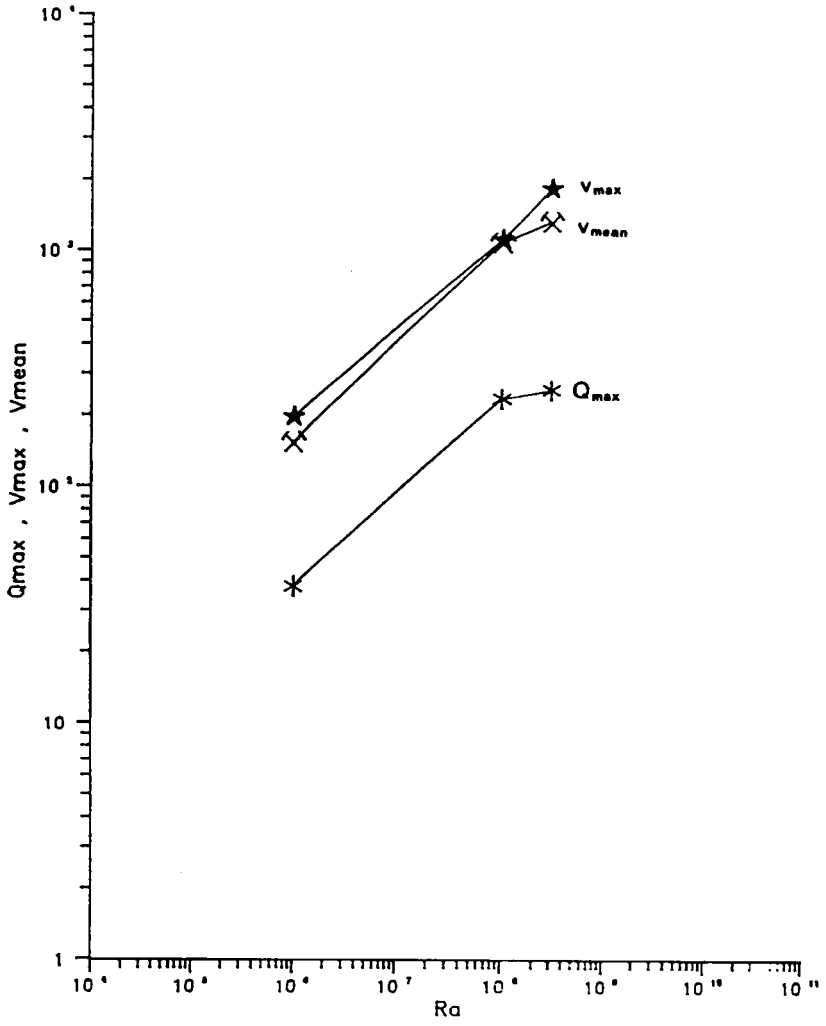

Figure 16(b). Dependence of dimensionless v_{max}, Q_{max} and v_{mean} on Ra for $Pr = 7$, $S = 0{\cdot}1$. The velocities have been normalized using a/h and the flow rate using a. The values corresponding to $Ra = 3{\cdot}1 \times 10^8$ have been measured experimentally (but for $S = 0{\cdot}086$ see chapter V)

A dimensionless length r_1 of a domain associated with a Rayleigh number value Ra_1 can be rescaled to using the length scale of a domain with value Ra_2 by

$$\frac{r_2}{r_1} = \left(\frac{Ra_2}{Ra_1}\right)^{1/4}. \tag{29}$$

Similarly, to rescale a dimensionless flow rate Q_1 from Ra_1 to Q_2 of Ra_2, the formula to be used is

$$\frac{Q_1}{Q_2} = \left(\frac{Ra_2}{Ra_1}\right)^{1/2}. \tag{30}$$

The comparison between the $Ra = 10^4$ and 10^6 Q-curves appears in Figure 17(a) and for $Ra = 10^6$, 10^8 in Figure 17(b).

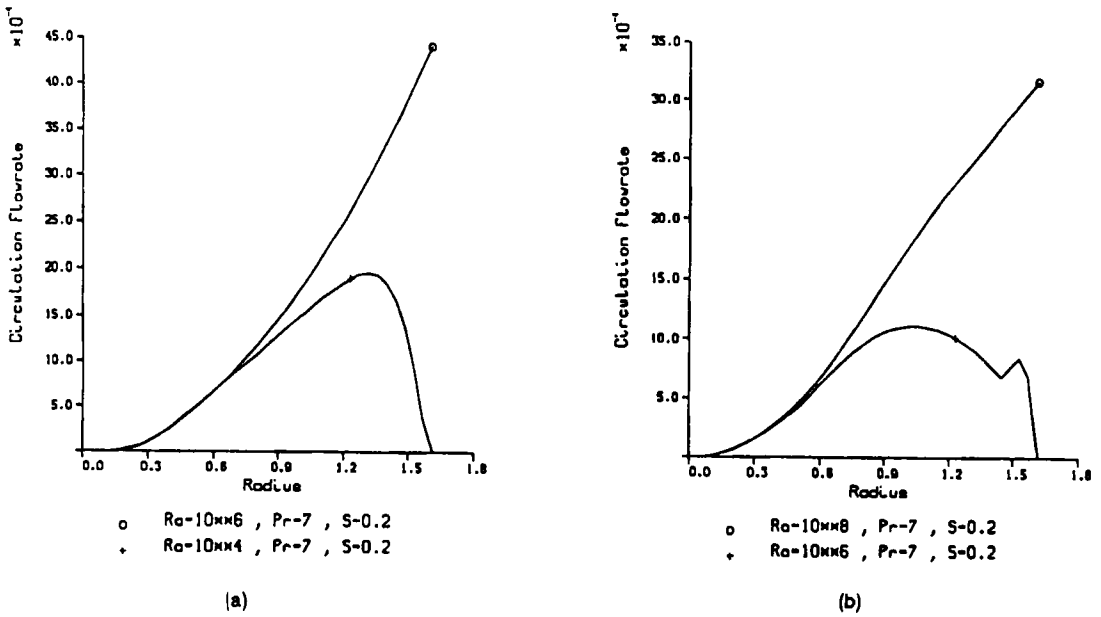

Figure 17. Comparison between Q-curves for (a) $Ra = 10^4$, 10^6 and (b) $Ra = 10^6$, 10^8 (time-averaged). In both cases the scales used correspond to the higher Ra

The most important outcome of the numerical solutions to be used in applications is the flow rate that develops at the deep end of the domain and establishes an exchange flow between the littoral and open waters. To extract the exchange flow rate from calculations or experiments in a closed-end domain, the linear portion of the Q-curves can be extrapolated up to the closed end. Figure 17 shows that such an extrapolation will tend to underestimate the exchange flow that would develop in an open-ended domain. Thus use of solutions to the model formulated in Section 2.1 in the analysis of cooling-induced exchange flow will produce low estimates.

Increase in surface heat loss rate H. Alternatively, an increase in Ra can be due to an increase in surface heat loss rate H while the fluid is specified and the maximum depth h is kept constant. In this case the flow rates have to be rescaled according to equation (10), while the lengths remain unchanged. To observe the qualitative influence of an increase in H on the flow quantities, the flow fields for $Ra = 10^4$, 10^6, 10^8 have been juxtaposed in Figure 18.

3.6. Dependence on slope

The effects that changes in slope have on the flow were investigated by comparing solutions at $Ra = 10^6$ and 10^8 with $Pr = 7$ for slopes $S = 0{\cdot}1$ and $0{\cdot}2$. In general it was found that within this range of the parameters, changes in slope did not alter the distinctive characteristics in the evolution and the steady state of the flow. For example, the secondary cell in the deep end of the domain at $Ra = 10^6$ was present at the steady state of both the $S = 0{\cdot}1$ and $0{\cdot}2$ solutions, and the same holds for the time-averaged fields at $Ra = 10^8$.

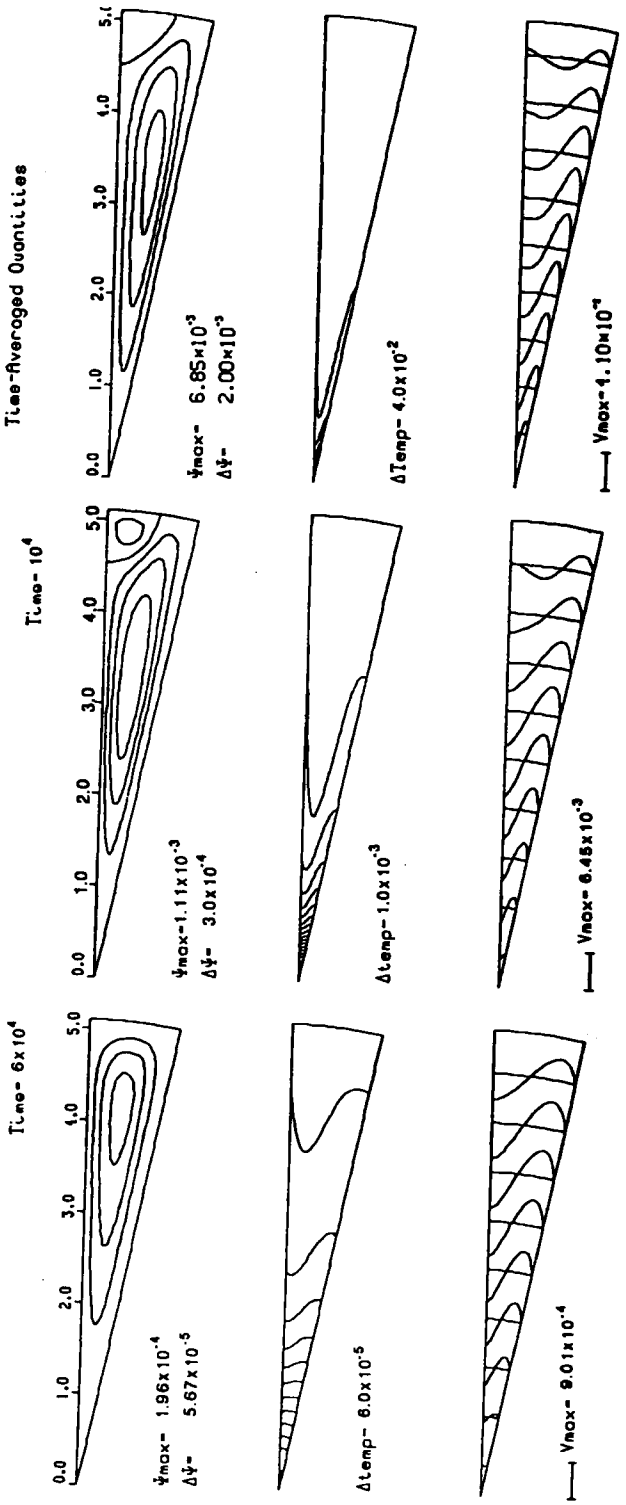

Figure 18. Comparison of streamlines, isotherms and radial velocity profiles for $Ra = 10^4$, 10^6, 10^8 (from left to right). All quantities have been scaled with $Ra = 10^8$ scales ($Pr = 7$, $S = 0{\cdot}2$ for all graphs)

Among the most interesting features of the model described in Sections 2.1 and 2.2 is the behaviour of the flow as the slope S decreases. It can be recalled from Section 2.3 that the steady, depth-integrated heat transfer is given by

$$\bar{H}_{st}(r) = Hr\left(\frac{r}{R} - 1\right), \tag{31}$$

so that the average heat transfer is

$$\frac{\bar{H}_{st}(r)}{rS} = H\left(\frac{r}{R} - 1\right)S^{-1}. \tag{32}$$

From equation (32) it follows that as $S \to 0$, the average horizontal heat transfer increases as S^{-1}. In Section 2.4 on pure conduction it was shown that as a result, as $S \to 0$, the horizontal temperature scale increases as S^{-2} (equation (27)). Scaling arguments indicate that there exists a flow region at the pointed end of the domain where heat transfer is dominated by conduction. The length of this region decreases as $S^{1/2}$ in the limit $S \to 0$. Thus it can be expected that the strength of advection increases as the slope decreases, and the advective terms in the energy equation become dominant, since as the slope decreases, the radial amount of heat flow imposed by the boundary conditions is forced through a 'shallower' depth.

The dependence of v_{max} and Q_{max} on S can be seen from the values included in Table IV. All values correspond to the $Pr = 7$ calculation except those marked by an asterisk, for which $Pr = 1$.

3.7. Time to steady state

The dimensionless time required to reach steady state is summarized in Table V as a function of Ra and S.

Table IV. Maximum normalized velocity and flow rate dependence on Rayleigh number and slope

	$V_{max}/(h/\alpha)$		Q_{max}/α	
Ra	$S = 0{\cdot}1$	$S = 0{\cdot}2$	$S = 0{\cdot}1$	$S = 0{\cdot}2$
10^4	26·5*	⇔↑·8	5·89*	5·19
10^6	195	171	37·6	29·4
10^8	1110	1020	234	166

Table V. Time to steady state, normalized by the h^2/α scale

Ra	$S = 0{\cdot}1$	$S = 0{\cdot}2$
10^4	5·0	2·0
10^6	0·5	0·2

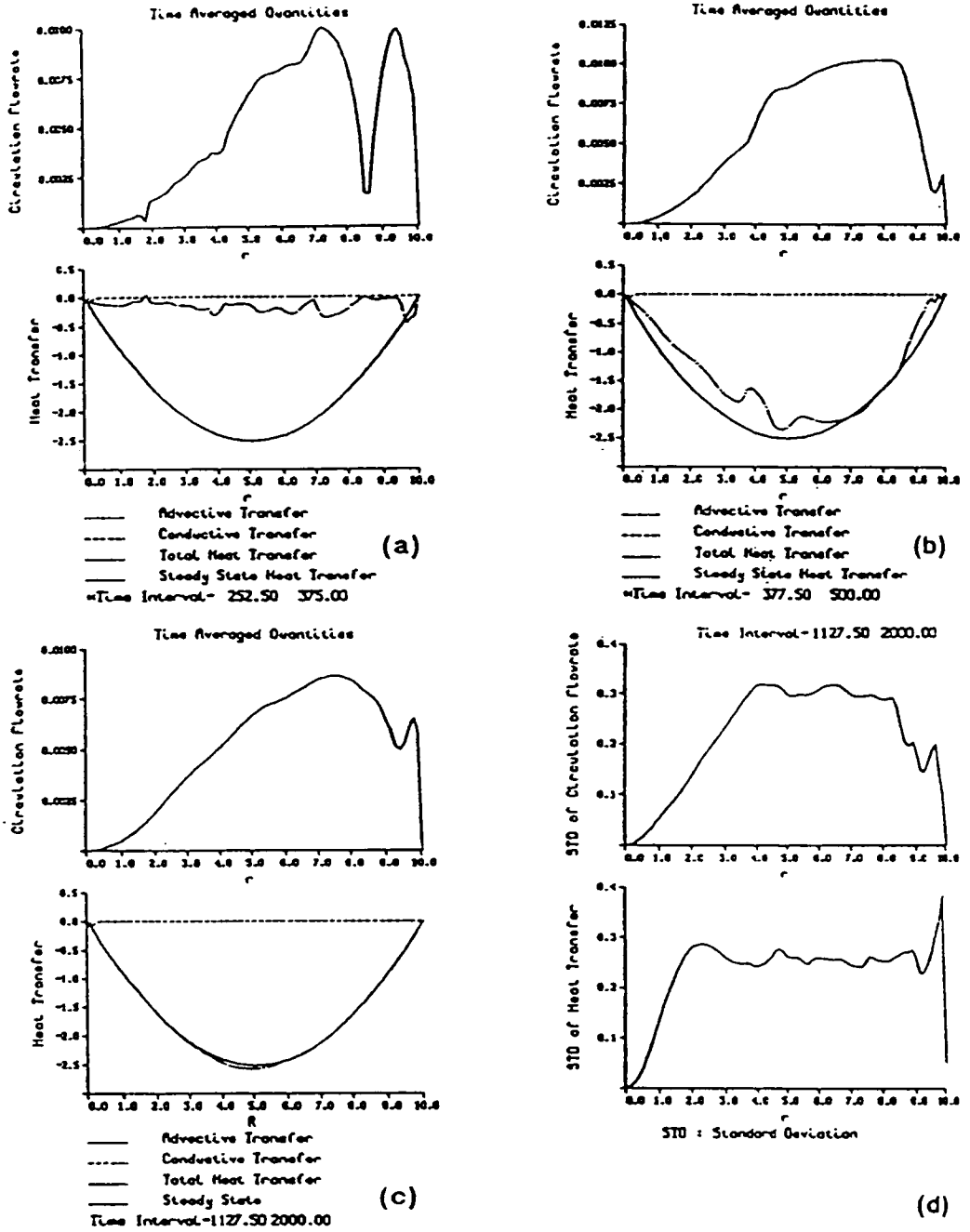

Figure 19. Averages for the $Ra = 10^8$, $Pr = 7$, $S = 0{\cdot}1$ solution. Improvement of the quality of the time-averaged curves as averaging is moved from (a) within to (b) outside the initial development period. (c) Time-averaged radial flow rate and heat transfer curves over a long interval and (d) the corresponding standard deviations

From Figures 4, 5, 7 and 8 it can be seen that the time to steady state consists of the time required to reach the single-cell configuration plus a diffusive adjustment necessary to reach the steady state heat transfer. At $Ra = 10^6$ this diffusive adjustment is simultaneous with oscillations in the flow field caused by the adjustment of the secondary cell at the deep end.

At $Ra = 10^8$, where the solutions reach a steady state in a time-averaged sense only, the important time scales are the length of an adequate time-averaging interval and the initial development interval, which should be excluded from the steady state averaging.

A suitable criterion for the adequacy of the length of time-averaging interval can be based on equation (22); the time-averaged flow rate curves are shown in Figure 14 for $Ra = 10^8$, $Pr = 7$, $S = 0{\cdot}2$ and in Figure 19 for $Ra = 10^8$, $Pr = 7$, $S = 0{\cdot}1$.

As the time-averaging interval is reduced, the averages deteriorate. To determine the time required for the initial development, averages were taken over intervals of fixed length but positioned at different instants within the calculated record. Using an interval of length $\Delta t = 125$, it was found that the qualities of the time-averaged radial flow rate and heat transfer curves change abruptly at $t \sim 400$, as is seen in Figure 19.

4. CONCLUSIONS

The thermal gravitational circulation in a two-dimensional wedge-like enclosure, insulated from the bottom and cooled from the surface, has been studied through numerical simulations. Interest in this formulation is stimulated by the desire to study convective currents which arise in the littoral region of lakes, where they provide a transport mechanism without affecting the stratification of the main lake. As a result of the imposed boundary conditions the horizontal temperature gradient develops internally, rather than being imposed as is the case with more traditional natural convection settings. It is found that as the Rayleigh number is increased, intermittent cells, which for low and intermediate Ra-values are present only during the initial evolution of the flow, survive at the (statistical) steady state, thus rendering the flow time-dependent. The flow is shown to be insensitive to Prandtl number changes (at high enough Pr-values), which implies that the advection terms in the momentum equations are of little importance.

ACKNOWLEDGEMENT

The Minnesota Supercomputer Institute, University of Minnesota provided a resource grant and access to its Cray 2 supercomputer for the initial development of this study.

REFERENCES

1. H. Stefan, G. Horsch and J. Barko, 'A model for the estimation of convection exchange in the littoral region of a shallow lake during cooling', *Hydrobiologia*, 174 (1989).
2. Patterson, 'A model for convective motions in reservoir sidearms', IAHR Congress, Lausanne, (1987).
3. G. M. Horsch and H. G. Stefan, 'Convective circulation in littoral water due to surface cooling', *Limnol. Oceanogr.*, **33**, 1068–1083 (1988).
4. S. Ostrach, 'Low-gravity fluid flows', *Ann. Rev. Fluid Mech.*, **14**, 313–345 (1982).
5. D. R. Moore and N. O. Weiss, 'Two-dimensional Rayleigh–Bénard convection', *J. Fluid Mech.*, **58**, 289–312 (1973).
6. J. Patterson and J. Imberger, 'Unsteady natural convection in a rectangular cavity', *J. Fluid Mech.*, **100**, 65–86 (1980).
7. D. Poulikakos and A. Bejan, 'The fluid dynamics of an attic space', *J. Fluid Mech.*, **131**, 251–269 (1983).
8. A. Bejan, *Convective Heat Transfer*, Wiley, New York, 1984.
9. G. M. Horsch and H. G. Stefan, 'Cooling-induced convective littoral currents in lakes: simulation and analysis', *Project Rep. 272*, St. Anthony Falls Hydraulic Laboratory, University of Minnesota, Minneapolis, MN, 1988.

10. S. V. Patankar and D. B. Spalding, 'A calculation procedure for heat, mass and momentum transfer in three-dimensional parabolic flows', *Int. J. Heat Mass Transfer*, **15**, 1787–1794 (1972).
11. S. V. Patankar, 'A calculation procedure for two-dimensional elliptic situations', *Numer. Heat Transfer*, **4**, 409–442 (1981).
12. S. V. Patankar, *A General Purpose Computer Program for Two-dimensional Elliptic Situations*, Mechanical Engineering Department, University of Minnesota, Minneapolis, MN, 1982.
13. Patankar, Numerical Heat Transfer and Fluid Flow, McGraw-Hill, New York, 1980.
14. G. De Vahl Davis, 'Laminar natural convection in an enclosed rectangular cavity', *Int. J. Heat Mass Transfer*, **11**, 1675–1693 (1968).
15. C. Quon, 'High Rayleigh number convection in an enclosure—a numerical study', *Phys. Fluids*, **15**, 12–19 (1972).
16. G. D. Mallinson and G. De Vahl Davis, 'Three-dimensional natural convection in a box: a numerical study', *J. Fluid Mech.*, **83**, 1–31 (1977).
17. F. H. Busse, 'Non-linear properties of thermal convection', *Rep. Prog. Phys.*, **41**, 1929–1967 (1978).
18. G. M. Horsch and H. G. Stefan, 'Cooling-induced natural convection in a triangular enclosure as a model for littoral circulation', in *Computational Methods in Water Resources*, Vol. 1, Elsevier, Amsterdam, 1988.
19. T. D. Foster, 'Intermittent convection', *Geophys. Fluid Dyn.*, **2**, 201–217 (1971).
20. T. D. Foster, 'Stability of a homogeneous fluid cooled uniformly from above', *Phys. Fluids*, **8**, 1249–1257 (1965).
21. T. D. Foster, 'Onset of convection in a layer of fluid cooled from above', *Phys. Fluids*, **8**, 1770–1774 (1965).
22. T. D. Foster, 'A convective model for the diurnal cycle in the upper ocean', *J. Geophys. Res.*, **76**, 666–675 (1971).
23. K. B. Katsaros, W. T. Liu, J. A. Businger and J. E. Tillman, 'Heat transport and thermal structure in the interfacial boundary layer in an open tank of water in turbulent free convection', *J. Fluid Mech.*, **83**, 311–336 (1977).
24. N. Tamai and T. Asaeda, 'Sheetlike plumes near a heated bottom plate at large Rayleigh number', *J. Geophys. Res.*, **89**, 727–734 (1984).
25. J. M. T. Thompson and H. B. Stewart, *Nonlinear Dynamics and Chaos*, Wiley, New York, 1987.
26. L. Kleiser and T. A. Zang, 'Numerical simulation of transition in wall bounded shear flows', *Ann. Rev. Fluid Mech.*, **23**, 495–537 (1991).